RESEARCH ARTICLE

Single-Actuator Hip Exoskeleton Mechanism Design With Actuation in Frontal and Sagittal Planes: Design Methodology and Experimental Validation

JONGJUN LEE[1], **JEGYEONG RYU**[1], **GYUIK LEE**[1], **JEONGHAN YU**[1], **SEOK WON KANG**[2], **AND YOON YOUNG KIM**[1]

[1]Department of Mechanical Engineering, Seoul National University, Seoul 08826, South Korea
[2]Department of Civil and Systems Engineering, Johns Hopkins University, Baltimore, MD 21218, USA

Corresponding authors: Yoon Young Kim (yykim@snu.ac.kr) and Seok Won Kang (skang74@jhu.edu)

ABSTRACT Most mobile-type hip exoskeletons only assist on a sagittal plane with a single actuator per hip joint for compactness, lightweightness, and low cost. Even though a new concept of hip mechanism that allows assistance not only on a sagittal plane but also on a frontal plane only with a single actuator has been proposed recently, it has several limitations, such as having a small range of motion and being applicable only on a single gait-mode. Herein, we propose a novel design approach that is a well-combined procedure of target design with clinical walking data, multi-objective design problem definition, type synthesis of mechanism, and analysis of the obtained Pareto-front solutions. We take the hip spherical mechanism's kinematic trade-offs into account. By utilizing a more complex type of 1-DOF(Degrees of Freedom) mechanism (6-bar Stephenson-III) and multi-objective optimization approach, we successfully enhanced both compactness and hip moment assistance in the single-actuator hip exoskeleton mechanism, and its performance was validated via benchtop experiment of its prototype.

I. INTRODUCTION

Lower-limb Exoskeleton technology has rapidly advanced, allowing the elderly and individuals with disabilities to regain independent mobility. Among the three major lower-limb joints – the hip, knee, and ankle – the hip joint has received considerable attention due to its capacity to provide the largest moment assistance while keeping external mass close to the proximal body [1], [2].

The leg performs a three-dimensional rotational motion centered around the hip joint, and three-dimensional moments generated by the muscles control this motion. The forward propulsion during walking mainly occurs by the sagittal plane moment. The majority of clinical research has

The associate editor coordinating the review of this manuscript and approving it for publication was Jingang Jiang.

Concept of 3-DOF Hip joint mechanism

1) 3-DOF Spherical mechanism synchronized with Leg motion

2) Output Moment direction transformed depending on hip angle

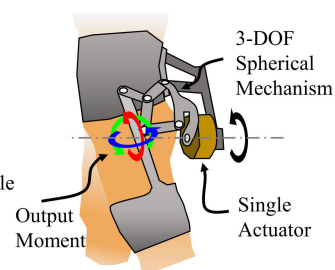3) 3-DOF assistive moment with Single actuator

FIGURE 1. Hip moment assistance concept using the 3-DOF hip joint mechanism.

concentrated on assisting sagittal plane moments, seeking appropriate moment patterns, magnitudes, and timing [3], [4], [5]. Nevertheless, research on exoskeletons assisting the

frontal plane, which contributes to stability and load-carrying during walking, has also progressed steadily. Biomechanical simulations have suggested that muscles involved in hip abduction (outward rotation on the frontal plane) are the most effective for reducing metabolism [6]. It has been proposed that an exoskeleton that assists the frontal plane can control the step width, improving walking stability [7], [8]. Thus, within the context of the three-dimensional moments governing walking, both the sagittal plane moment contributing to forward propulsion and the frontal plane moment contributing to stability are essential.

Numerous exoskeleton designs have been proposed to assist both sagittal and frontal plane moments. However, assisting both planes necessitates the attachment of at least four actuators, introducing a weight-related drawback. Some designs have employed two actuators to control each plane directly [9], while others have incorporated mechanisms to transform the multiple input moments into desired directions of output moments [10], [11], [12].

Kang et al. on the other hand, introduced a 'R-4B-R' 3-DOF spherical mechanism to assist both planes using only a single actuator [13]. This mechanism achieves variability in assisting the sagittal plane moments by designing the location of the Instantaneous Center of Rotation (ICOR) of a 4-bar mechanism while maintaining constant frontal plane moments. Due to the characteristics of this mechanism, when the direction of the output moment is well-designed, one can expect enhanced assistive performance with a lightweight structure. However, Kang's proposal had several limitations. Firstly, when specifying the direction of the transformed output moment, it did not take into account the human biological moments required in a person's actual walking environment. As a result, the magnitude of moments in the sagittal plane produced by the mechanism was not properly adjusted to biological moments in terms of both magnitude and direction at each gait time segment. Additionally, the designed height of the mechanism was too high, restricting step width during walking and compromising stability.

The objective of this study is to develop a mechanism design methodology that overcomes these limitations in a frontal and sagittal assistance hip mechanism driven by a single actuator, thereby achieving high assistive performance.

Firstly, we designed the mechanism to align the direction of the output moments with the required biomechanical moments in real walking environments. Real walking environments encompass not only level ground walking but also various inclines. To achieve this, we defined the target output moments of the mechanism by considering both level ground walking and the standard maximum slope specified by the Americans with Disabilities Act (ADA), which is 5° [14]. Additionally, we designed the mechanism with a maximum height constraint to ensure the size of the step width.

Secondly, in this study, we employed a 6-bar Stephenson-III mechanism instead of a 4-bar mechanism. This 1-DOF mechanism possesses a more intricate ICOR (Instantaneous Center of Rotation) trajectory, allowing the 'R-6SB-R'

mechanism to provide a wider range of sagittal plane moments while maintaining compact volume [15].

Lastly, our study incorporates a multi-objective design optimization, taking into account the trade-off relationship between sagittal moment range and mechanism compactness. Through this approach, we have obtained three distinct solution groups, each demonstrating superior performance in different aspects. We analyzed these three representative mechanisms within each group and validated their superior performance compared to the original R-4B-R mechanism. Additionally, we developed a robot prototype and a testing bench to verify that the mechanism can indeed produce the desired moments in the intended directions with a single actuator.

The contributions of this study are as follows:

1) We overcame several technical challenges of a single-actuator-driven hip exoskeleton robot mechanism to assist frontal and sagittal planes with novel design methodology. Our approach set the design problem with consideration of biological requirements with clinical walking data, exploring design possibilities with a multi-objective optimization algorithm, resulting in the mechanism's output moments aligned with the biological moment profile.

2) Furthermore, we validated the robot's outputs using a testing bench equipped with a artificial thigh model, confirming that the robot's performance closely matches theoretical expectations. Notably, among all exoskeletons designed to assist both the sagittal and frontal planes, this concept of robot is expected to be the lightest when considering the equivalent size of the actuator.

The rest of this paper is organized as follows. Section II shows the definition of the target performance of a single-actuator sagittal and frontal plane assisting hip mechanism. Section III describes the modeling of the selected R-6SB-R type mechanism and its principle of converting output moment. Section IV shows the multi-objective optimization formulation, the selected algorithm(NSGA-II), and the design optimization process. Section V shows the result analysis of the design optimization. Section VI shows the realization of the hip mechanism, test bench system, and experimental results. Section VII presents the conclusions of the study.

II. TARGET PERFORMANCE DEFINITION OF SINGLE-ACTUATOR HIP EXOSKELETON MECHANISM
A. BIOMECHANICAL TARGET MOMENT

In order to design the Single-Actuator Hip Exoskeleton Mechanism, a target moment trajectory is required. Previous clinical studies have revealed that the optimal assistance strategy for exoskeleton robots closely aligns with the timing of a person's biomechanical moments [4], [5]. Thus, we assumed that providing effective assistance in walking could be achieved when the output moments of the
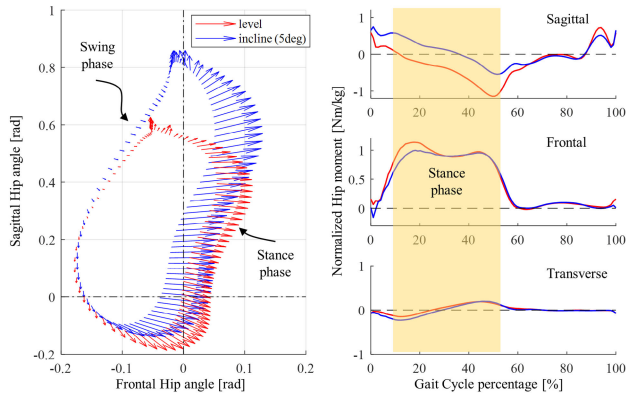
FIGURE 2. Biological Hip Moment at level walking and incline walking. Most moment maintaining walking motion occurs in the stance phase in both cases.

TABLE 1. the specifications of the biological target moment.

	level walking			incline walking		
t^*	$\hat{m}_{t^*}^{sag}$	$\hat{m}_{t^*}^{frt}$	$\hat{m}_{t^*}^{trv}$	$\hat{m}_{t^*}^{sag}$	$\hat{m}_{t^*}^{frt}$	$\hat{m}_{t^*}^{trv}$
10	0.108	0.783	-0.122	0.578	0.619	-0.205
11	0.062	0.873	-0.134	0.573	0.689	-0.221
12	0.027	0.965	-0.145	0.553	0.764	-0.228
13	-0.019	1.032	-0.148	0.518	0.821	-0.229
14	-0.066	1.065	-0.147	0.490	0.860	-0.226
15	-0.106	1.107	-0.141	0.461	0.908	-0.220
16	-0.132	1.118	-0.134	0.430	0.940	-0.213
17	-0.154	1.130	-0.124	0.398	0.965	-0.203
18	-0.173	1.136	-0.111	0.362	0.989	-0.185
19	-0.191	1.136	-0.098	0.327	0.998	-0.171
20	-0.210	1.132	-0.083	0.292	0.986	-0.156
21	-0.227	1.119	-0.069	0.262	0.991	-0.134
22	-0.246	1.093	-0.052	0.235	0.976	-0.120
23	-0.264	1.061	-0.038	0.217	0.964	-0.103
24	-0.277	1.034	-0.022	0.204	0.960	-0.085
25	-0.292	1.007	-0.008	0.196	0.955	-0.071
26	-0.305	0.984	0.006	0.185	0.942	-0.054
27	-0.316	0.958	0.018	0.174	0.924	-0.040
28	-0.326	0.939	0.031	0.164	0.915	-0.024
29	-0.337	0.925	0.044	0.152	0.907	-0.010
30	-0.351	0.911	0.056	0.141	0.901	0.003
31	-0.367	0.901	0.067	0.125	0.897	0.016
32	-0.389	0.894	0.078	0.109	0.897	0.033
33	-0.414	0.889	0.090	0.092	0.893	0.044
34	-0.443	0.885	0.101	0.070	0.896	0.060
35	-0.476	0.887	0.113	0.048	0.900	0.076
36	-0.511	0.890	0.124	0.022	0.901	0.087
37	-0.547	0.893	0.135	-0.007	0.909	0.104
38	-0.586	0.898	0.144	-0.035	0.912	0.117
39	-0.627	0.910	0.155	-0.063	0.917	0.130
40	-0.666	0.925	0.165	-0.092	0.924	0.145
41	-0.711	0.940	0.173	-0.118	0.930	0.155
42	-0.758	0.954	0.180	-0.146	0.936	0.167
43	-0.809	0.966	0.185	-0.180	0.945	0.179
44	-0.863	0.974	0.190	-0.220	0.952	0.186
45	-0.918	0.974	0.191	-0.267	0.953	0.191
46	-0.976	0.961	0.189	-0.317	0.948	0.199
47	-1.031	0.941	0.185	-0.371	0.933	0.198
48	-1.079	0.913	0.178	-0.423	0.908	0.196
49	-1.120	0.874	0.170	-0.471	0.877	0.195
50	-1.144	0.824	0.159	-0.510	0.830	0.182
51	-1.145	0.758	0.146	-0.536	0.775	0.169
52	-1.112	0.675	0.131	-0.548	0.708	0.154

t^* is discrete-time in gait cycle percentage.
All hip moments $\hat{m}_{t^*}$ in this paper are normalized, (Nm/kg).

mechanism closely mirror the biomechanical moments. For this purpose, we utilized the averaged clinical data of walking moments from ten able-bodied individuals on level ground and a 5° incline as our target moments [14].

Fig. 2 illustrates the magnitude and direction of hip biomechanical moments based on the trajectory of a hip angle during walking. Walking consists of the stance phase, which begins with 'heel strike' as the reference point, where the foot makes contact with the ground and moves backward, and the swing phase, which starts at 50% of the gait cycle at 'toe-off', where the leg moves forward while in the air. It's worth noting that dominant moments in both the frontal and sagittal planes occur during the stance phase. Consequently, we have limited the temporal range of the target moments to the stance phase. For detailed specifications of the target moments, see Table 1. Additionally, we have positioned the actuator at the back of the user in the frontal plane. Therefore, the mechanism is designed such that the input moments are proportional to the magnitude of frontal plane biomechanical moments.

Furthermore, the right side of Fig. 2 illustrates the moment components as a function of GCP(Gait Cycle Percentage). It is evident that the magnitude of the transverse plane moment is much smaller compared to the frontal and sagittal plane moments. We have constrained the transverse plane moment to be zero. We will discuss the optimization formulation in detail in Section IV.

Level walking and incline walking exhibit different hip angle trajectories, with incline walking having a broader trajectory, particularly in the sagittal plane. We have chosen to use both trajectories as targets. Accordingly, the mechanism's output moments are configured to follow an intermediate direction where the targets overlap and to align with the incline walking moment at extreme forward angles.

B. MECHANISM COMPACTNESS

Fig. 3(a) illustrates the presented R-6SB-R mechanism in its worn state. Joints 2 and 8 of this mechanism have the highest altitude. The altitude of joints varies depending

on the mechanism's motion, and if it is too high, the exoskeleton mechanism may encroach on the waist, resulting in limited motion in the frontal plane and diminished output moments. Therefore, we have designed the 'compactness' cost function which is defined by the highest altitude of all joints. Further details will be discussed in Section IV's optimization formulation.

III. NEW 'R-6SB-R' SINGLE-ACTUATOR HIP MECHANISM
A. TYPE SYNTHESIS: 6-BAR STEPHENSON-III MECHANISM

While maintaining the operational principles of Kang's proposed 'R-4B-R' Single-Actuator Hip Mechanism, we have employed a 6-bar Stephenson-III mechanism to achieve a broader range of sagittal plane moments while keeping the

the mechanism compact. Following the 4-bar configuration, the more complex 1-DOF mechanism is the 6-bar mechanism and there are a total of five types (Watt-I, Watt-II, Stephenson-I, Stephenson-II, Stephenson-III) in the 6-bar. Sancibrian and colleagues has suggested that the 6-bar Stephenson-III type provides a more versatile linkage that the four-bar type cannot approximate very effectively, especially when dealing with problems related to ICOR trajectories [15]. Additionally, we have determined that the Stephenson-III type requires the fewest number of linkage layers(5 layers), to realize the robot mechanism. As a result, we have chosen the Stephenson-III type as the most suitable option.

B. KINEMATIC ANALYSIS OF R-6SB-R MECHANISM

Fig. 3 displays the proposed R-6SB-R Single-Actuator Hip Mechanism. This mechanism consists of two revolute joints (R1, R8) and one 1-DOF 6-bar Stephenson-III mechanism consisting of six revolute joints (R2-R7).

Fig. 3(b) illustrates the design variables of the R-6SB-R mechanism. There are a total of 12 design variables $l_1 - l_{12}$, representing the lengths (spherical angles) of the links connecting the joints. We analyzed the mechanism configurations by using a quasi-static approach, where the position of the end-effector link connected to joint R8, determined by the given hip joint angle, is used to find the positions of the remaining links while satisfying joint compatibility conditions.

Fig. 3(c) depicts the virtual link formed by IR2 and R8 in the R-6SB-R mechanism. In the given configuration, the 6-bar Stephenson-III mechanism instantaneously rotates about a virtual axis connecting the Instantaneous Center of Rotation, denoted as IR2 [16], and the center of the sphere. IR2 is the intersection point of the extrapolation lines formed by a link connecting the joint R2 and IR1 and the link connecting joint R3 and R4. IR1, on the other hand, is the intersection point of the extrapolation lines created by the R6-R5 link and the R7-R4 link. The Location IR1 and IR2 are expressed as

$$\mathbf{r}_{I1} = \frac{(\mathbf{r}_6 \times \mathbf{r}_5) \times (\mathbf{r}_7 \times \mathbf{r}_4)}{\|(\mathbf{r}_6 \times \mathbf{r}_5) \times (\mathbf{r}_7 \times \mathbf{r}_4)\|}, \tag{1}$$

$$\mathbf{r}_{I2} = \frac{(\mathbf{r}_2 \times \mathbf{r}_{I1}) \times (\mathbf{r}_3 \times \mathbf{r}_4)}{\|(\mathbf{r}_2 \times \mathbf{r}_{I1}) \times (\mathbf{r}_3 \times \mathbf{r}_4)\|}, \tag{2}$$

where $\mathbf{r}_j$ is the unit position vector of the joint j. The direction and magnitude of the output moment is expressed as

$$\frac{\mathbf{M}_{out}}{\|\mathbf{M}_{out}\|} = \frac{\mathbf{r}_{I2} \times \mathbf{r}_8}{\|\mathbf{r}_{I2} \times \mathbf{r}_8\|}, \tag{3}$$

$$\|\mathbf{M}_{out}\| = \frac{\|\mathbf{M}_{inp}\|}{(\mathbf{M}_{inp}/\|\mathbf{M}_{inp}\|) \times (\mathbf{M}_{out}/\|\mathbf{M}_{out}\|)}. \tag{4}$$

Since the direction of the moment is determined as the direction perpendicular to a plane formed by the virtual link, indicated by the red line in Fig. 3(c), and the center of the sphere, we can infer the direction of the moment from the virtual link.

IV. MULTI-OBJECTIVE DESIGN OPTIMIZATION
A. FORMULATION
The design variables ξ_i is ξ_i ($0 < \xi_i < 1$, $i = 1, 2, \cdots, N_L$), N_L represents the number of links in the mechanism. ξ_i is the normalized link length l_i, described as

$$\xi_i = \frac{l_i - l_{initial}}{l_{initial}}. \tag{5}$$

The variable l_i is the lengths(same as the central angle of the sphere) of the links as shown in Fig. 3(b). The initial values l_i are set to match the positions of the joints in the existing R-4B-R, except for joints R6 and R7, and these values can be found in Table 2.

The formulation for optimization is expressed as

$$\begin{aligned}
&\text{Find} \quad \xi \\
&\underset{\xi}{\text{argmin}} \quad \{J_1, J_2, J_3\} \\
&\text{subject to} \quad [\Psi_s]_{t^*} \leq \epsilon \\
&\qquad\qquad\quad [\Psi_{frt}]_{t^*} \leq \epsilon \\
&\qquad\qquad\quad [\Psi_{trv}]_{t^*} \leq \epsilon
\end{aligned} \tag{6}$$

Firstly, an objective function J_1 represents moment direction consistency, defined as the average error in the direction of the target moment. The objective function J_1 is described as

$$J_1 = \sum_{t^*} \left\| \mathbf{M}_{out,t^*}\big|_{level} - \hat{\mathbf{M}}_{out,t^*}\big|_{level} \right\| \\
+ \sum_{t^*} \left\| \mathbf{M}_{out,t^*}\big|_{incline} - \hat{\mathbf{M}}_{out,t^*}\big|_{incline} \right\|. \tag{7}$$

The moment vector $\mathbf{M}_{out,t^*}$ represents the mechanism's output moment at time t^*. The time $t^* \in \{t^*|t^* = 10, 11, \cdots, 55\}$ corresponds to the sampled time in the stance phase. The moment vector $\hat{\mathbf{M}}_{out,t^*}\big|_{level}$ is the target biomechanical moment at time t^* during level walking. The moment vector $\hat{\mathbf{M}}\big|_{incline}$ represents the target biomechanical moment at time t^* during incline walking. The objective function J_1 decreases in value as the alignment between biomechanical moments and mechanism output moments improves.

An objective function J_2 takes a smaller value when the range of the sagittal direction in the mechanism's output moments is larger. The objective function J_2 is expressed as

$$J_2 = \frac{\hat{\Delta}\big|_{level} - \Delta\big|_{level}}{\hat{\Delta}\big|_{level}} + \frac{\hat{\Delta}\big|_{incline} - \Delta\big|_{incline}}{\hat{\Delta}\big|_{incline}}, \tag{8}$$

where

$$\Delta = \max_{t^*}(m_{out,t^*}^{sag}) - \min_{t^*}(m_{out,t^*}^{sag}). \tag{9}$$

The symbol Δ in equations (8) and (9) represents the range of moment components in the sagittal plane and is calculated as the difference between the maximum and minimum values of the sagittal plane moment components.

The symbol $\hat{\Delta}$ represents the difference between the maximum and minimum values of the sagittal plane moment
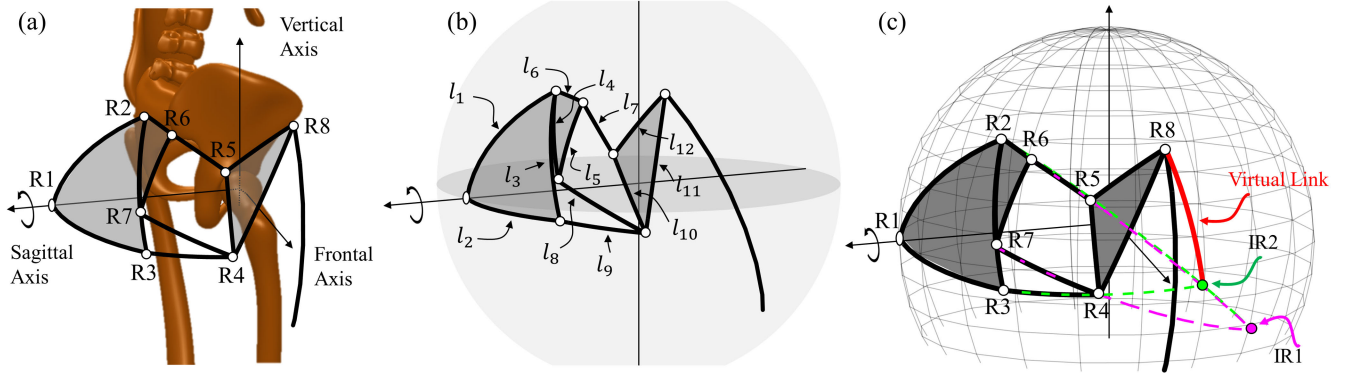
FIGURE 3. Representation of 3-DOF Hip mechanism. (a) The proposed R-6SB-R mechanism attached around the hip joint. (b) The design variables of the R-6SB-R mechanism. (c) Kinematic Analysis of R-6SB-R mechanism. According to the kinematic property of the Stephenson-III 6-bar mechanism, the mechanism's output moment is instantaneously defined by the virtual link's posture.

components in the target biological moment. The vector $\mathbf{m}_{out}^{sag}$ refers to the sagittal plane component of the mechanism's output moment $\mathbf{M_{out}} = [\mathbf{m}_{out}^{sag}, \mathbf{m}_{out}^{frt}, \mathbf{m}_{out}^{trv}]$. The objective function J_2 is designed to complement J_1 by ensuring that the mechanism's output moments are not biased towards smaller values, while still satisfying the moment direction consistency.

The objective function J_3 defines the compactness performance of the mechanism, expressed as

$$J_3 = \sum_{t^*} \max_j(\{\theta_{j,t^*}\big|_{level}, \theta_{j,t^*}\big|_{incline}\}). \quad (10)$$

The angle θ_{j,t^*} represents the altitude of joint j at time t^*. The objective function J_3 is calculated with respect to the highest angle among all joints, and a lower value of the objective function indicates that the mechanism has a more compact volume.

The constraint $\Psi_\mathbf{s}$ in formulation (6) is introduced to avoid the singularity of the mechanism, described as

$$[\Psi_s]_{t^*} = V(t_0) \times V(t^*) > \epsilon. \quad (11)$$

We used the method employed in previous research on the R-4B-R design [17]. If the sign of V changes, the mechanism is considered singular. $V(t^*)$ represents a volume created by three joints, R1, R8, and RI2, which generate output moments at the stance phase time t^*. The start of the gait cycle is used as t_0.

The constraint Ψ_{frt} in formulation (5) is related to the magnitude of frontal plane moments, described as

$$[\Psi_\mathbf{frt}]_{t^*} = \big|\mathbf{m}_{out,t^*}^{frt} + 1\big| - \mathbf{m}_{thres}^{frt} \leq \epsilon. \quad (12)$$

We established a constraint to maintain $\mathbf{m}_{out,t^*}^{frt}$ at a value of -1, meaning that the mechanism is designed to output the input moment generated behind it in a clockwise direction. By doing so, it is possible to control the input moment based on the pattern of frontal plane biological moments. The threshold value, m_{thres}^{frt}, is set to $1.5e-2$. Epsilon is commonly set to $1e-3$.
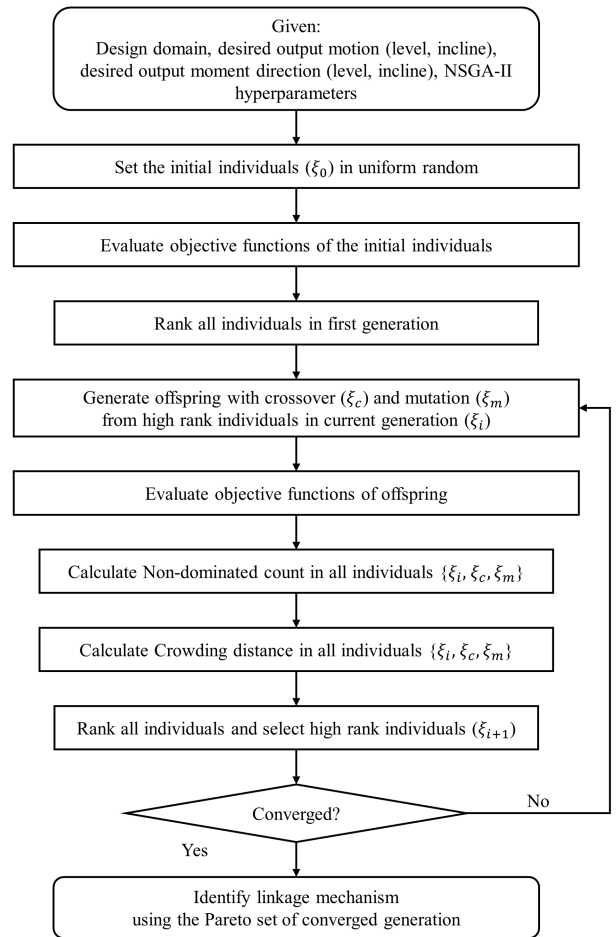

FIGURE 4. Flowchart of the design optimization process using NSGA-II. NSGA-II gives a Pareto-optimal front in Multi-Objective design problems by using a non-dominated rank system.

The constraint Ψ_{trv} in formulation (6) for suppressing transverse plane moments, described as

$$[\Psi_{trv}]_{t^*} = \big|\mathbf{m}_{out,t^*}^{trv}\big| - \mathbf{m}_{thres}^{trv} \leq \epsilon. \quad (13)$$

The target value is 0. m_{thres}^{trv} is set to 0.25, which is close to the maximum value of biological moments. If set too small, the penalty effect of the constraint becomes too strong, preventing the Pareto group from having a sufficiently diverse set of solutions.

B. NSGA-II ALGORITHM

In this study, we performed multi-objective design optimization to get Pareto-front solutions of the hip mechanism where objectives are direction and range of the output moments and compactness while meeting constraints. Here, the NSGA-II algorithm [18] is used for this optimization. Meanwhile, the penalty method is further utilized to deal with the constraints in (6). In the previous research, the mechanism synthesis problem using NSGA-II also handled constraints using the penalty method [19]. Some research has suggested that the 'Dynamic Joines (DJ)' penalty method [20] is particularly effective for handling constraints in NSGA-II [21]. Therefore, we transform the formulation (6) into the following form:

$$\text{Find} \quad \xi$$
$$\underset{\xi}{\text{argmin}} \quad \{f_1, f_2, f_3\} \tag{14}$$

where

$$f_i = J_i + (C \cdot t)^\alpha \sum_\gamma |\Psi_\gamma|^\beta.$$
$$(i = 1, 2, 3, \quad \gamma \in \{s, frt, trv\}) \tag{15}$$

In equation (15), the value t denotes iteration number, and the coefficients α, β, and C are set as proposed in [21]:

$$C = 0.5, \quad \alpha = 1, \quad \beta = 1$$

Consequently, dynamic penalties increase with iterations imposed on the objective functions f_i in (15).

The flowchart of the NSGA-II algorithm is shown in Fig. 4 and the fundamental concepts are as follows. Firstly, a randomly generated initial population is created and the objective function of each individual is evaluated. After non-dominated sorting, the genetic algorithm's basic operations, including selection, crossover(ξ_c), and mutation(ξ_m), are used to generate the first-generation population. Starting from the second generation, based on the non-dominated relationship and the density of individuals ξ_i, appropriate individuals are selected, and a new parent population is created. Basic genetic algorithm operations are employed to generate offspring populations. Finally, parent populations are merged with offspring populations $\{\xi_i, \xi_c, \xi_m\}$, non-dominated sorting is performed and high-rank individuals are selected (ξ_{i+1}). This process continues until the termination condition of the algorithm is met.

The NSGA-II parameters we used are as follows: a population size of 150 (10 times of the number of design variables), a generation count of 150 (same as population size), a crossover percentage of 70%, and a mutation percentage of 40%, and mutation probability of 3%.
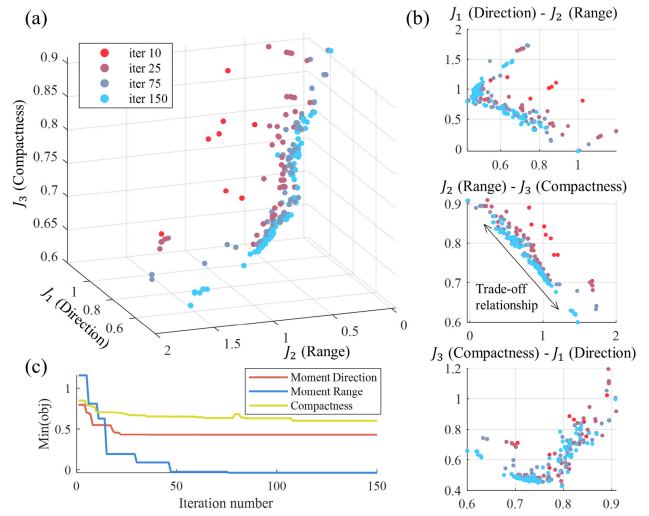

FIGURE 5. History of the proposed design process. (a) Pareto front solution history in 3-dimensional objective function space. (b) Iteration history of minimal value in each generation (c) Pareto front solution history in 2-dimensional objective function space. 2nd and 3rd objective have a trade-off relationship whereas the others have a U-shaped solution set.

C. DESIGN OPTIMIZATION RESULT

Fig. 5 illustrates the design process of the mechanism using NSGA-II. As the iterations progress, the number of solutions in the Pareto front group increases. By the 150_{th} iteration, all solutions have become part of the Pareto front. The iteration history shows the minimum values of each objective function at each iteration. It can be observed that there was no update in the minimum values for approximately the first 50 iterations before convergence. This indicates that over 150 iterations, the Pareto front group became sufficiently stable and wide, preventing newly created offspring solutions from dominating existing individuals.

In Fig. 5(b), when examining the shape of the Pareto front, it can be observed that there is a linear trade-off relationship between J_2 (range) and J_3 (compactness), while the other two combinations exhibit nonlinear trade-offs. This confirms that this multi-objective design problem is a nontrivial case, ensuring that additional subjective preferences can be applied to obtain the desired design from the obtained solution group.

In this study, we have clustered the final solution group into three major clusters and selected the featured solutions from each group, denoted as case 1, 2, 3. The clustering technique uses standard k-means clustering. Fig. 6(a) illustrates the convergence of the Pareto front into three groups. The U-shaped Pareto front lying on the diagonal plane can be divided into three groups where one of the objective functions significantly dominates. Fig. 7 compares the average objective function values of these three groups with the objectives of the original designs. Each group excels in its major objective compared to the other groups. In the case of the range group, it outperforms the R-4B-R mechanism
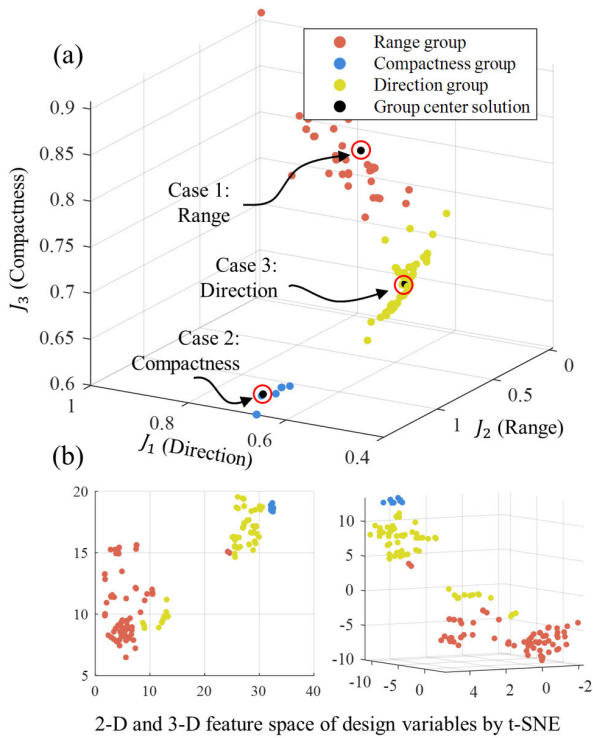
FIGURE 6. Result of the proposed design process. (a) Three groups of Pareto front solutions space. The design case of the center position of each group was analyzed representatively. (b) Each group in feature space using t-SNE dimension reduction technique.
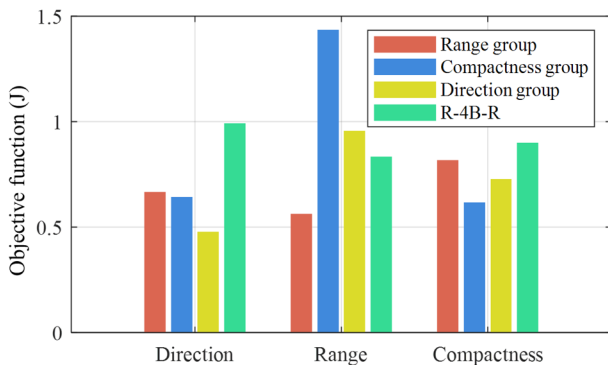

FIGURE 7. Performance overview of the representative case of each group. Since the objective functions are cost functions, the lower is the better. Each case has the best performance in major objective.

in all aspects. Meanwhile, the compactness group exhibits a significantly lower sagittal range but achieves high moment direction accuracy.

Additionally, we observed that the three groups also form somewhat similar clusters in the 12-dimensional design space. Fig. 6(b) shows the feature space of design variables reduced using t-SNE. Although there is some overlap between the range group and the direction group, we confirmed that each group exhibits a stable design variance within the same property group.

TABLE 2. The specifications of the R-6SB-R design variable.

					link length (central angle [°])							
	l_1	l_2	l_3	l_4	l_5	l_6	l_7	l_8	l_9	l_{10}	l_{11}	l_{12}
Initial	58.4	51.7	45.9	30.4	23.5	11.2	21.6	32.3	27.7	29.5	42.8	21.7
Case 1	46.2	33.9	44.0	37.8	28.3	11.5	21.4	32.4	22.3	35.1	57.0	19.0
Case 2	57.7	61.6	38.4	32.4	27.7	11.8	20.6	32.5	22.7	34.6	51.3	13.6
Case 3	45.8	49.9	39.6	31.0	28.3	12.1	21.0	32.3	21.2	33.3	59.7	15.6

						design variable						
	ξ_1	ξ_2	ξ_3	ξ_4	ξ_5	ξ_6	ξ_7	ξ_8	ξ_9	ξ_{10}	ξ_{11}	ξ_{12}
Initial	0.50	0.50	0.50	0.50	0.50	0.50	0.50	0.50	0.50	0.50	0.50	0.50
Case 1	0.40	0.33	0.48	0.62	0.60	0.51	0.50	0.50	0.40	0.59	0.67	0.44
Case 2	0.49	0.60	0.42	0.53	0.59	0.53	0.48	0.50	0.41	0.59	0.60	0.31
Case 3	0.39	0.48	0.43	0.51	0.60	0.54	0.49	0.50	0.38	0.56	0.70	0.36

*All hip moments in this paper are normalized, (Nm/kg).

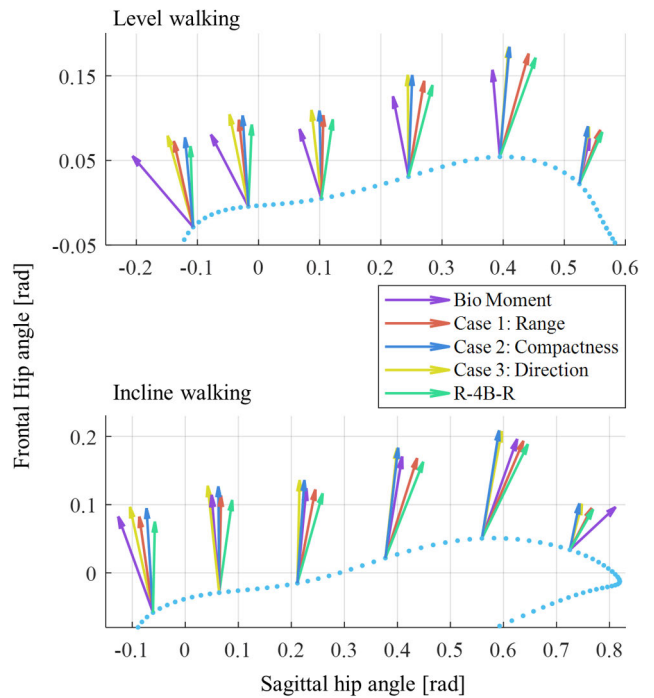**FIGURE 8.** Comparison of the output moment direction in hip angle space at stance phase. The solid blue line represents the hip angle trajectory.

V. KINEMATIC ANALYSIS OF DESIGNED MECHANISMS

All solutions on the Pareto front are equally good, but for analysis purposes, we have selected design solutions at the center of each group in the objective function space as representative cases for each group. We aim to compare these representative designs with the previously designed R-4B-R mechanism [13] in terms of output moment, ICOR, and compactness in the following sections, respectively. The specifications for the representative designs are given in Table 2.

A. MECHANISM OUTPUT MOMENT ANALYSIS

Fig. 8 illustrates a comparison of the output moment directions in the hip angle space during the stance phase. The dotted blue line represents the hip angle trajectory. The arrows

at each point represent the direction of the mechanism's output moment. It can be observed that the direction of the target biomechanical moment differs between level walking and incline walking, with a noticeable difference in the sagittal plane while the frontal plane moment remains dominant.

Case 1(Range) mechanism is oriented to have a large positive sagittal moment at a high sagittal angle. This helps maintain the leg extended forward during the early stance phase, making it more suitable for incline walking than level ground. Conversely, both level and incline walking scenarios commonly require a significant negative sagittal moment at negative sagittal angles, particularly during the push-off phase at the end of the stance phase, which generates powerful forward propulsion. Case 3(Direction) mechanism features the largest negative sagittal moment, which can provide strong assistive effects during this phase. Case 2(Compactness) mechanism primarily provides frontal plane moments in all situations, lacking a significant advantage in terms of output moment in specific scenarios.

These characteristics are more clearly evident in Fig. 9, which illustrates the mechanism's output moments during level and incline walking as a function of GCP. Specifically, the sagittal plane characteristics of each mechanism are pronounced. All mechanisms exhibit positive moments in the GCP range of 0-20% and negative moments in the range of 40-60%. However, R-4B-R is biased towards positive moments, while case 3(direction) mechanism is biased towards negative moments. On the other hand, case 1(range) mechanism does not have the largest moments in either range but displays a balanced assistive effect. Similarly, case 2(compact) mechanism also exhibits a balanced effect but with smaller moments on both sides.

Fig. 10 illustrates the output moments of each mechanism as a function of the input moment, given the size of the normalized biological moment. The graph takes into account the characteristics of hip frontal plane moments and forms a double-humped shape. In all mechanisms, the frontal plane moments are close to 1. As mentioned earlier, R-4B-R and case 3 (direction mechanism) show biased tendencies, while case 1 (range mechanism) and case 2 (compact mechanism) exhibit a balanced output.

B. ICOR AND VIRTUAL LINK ANALYSIS

In this study, we used a Stephenson-III type mechanism to overcome the limitations of a simple ICOR trajectory in the 4-bar linkage mechanism of R-4B-R [13] and to achieve a wider range of sagittal plane moments while maintaining a compact volume. In this part, we aim to analyze the virtual link to demonstrate the causes and tendencies of moment output.

Fig. 11 illustrates each mechanism's virtual link formed by IR2 and R8. Each time point is shown at intervals of 6% GCP from 1% to 50%. The behavior of joint R8 which is connected to the end-effector does not extend significantly beyond that of the original R-4B-R. However, the movement of

IR2 is more expansive, demonstrating a wider and narrower range based on design objectives. Specifically, case 1 (range mechanism) shows the widest virtual link range. However, as we move to the right, the limited range of R8 compared to IR2 causes the virtual link to tilt and not maintain vertical alignment, resulting in limitations in the lateral range of the virtual link.

C. COMPACTNESS ANALYSIS

Fig. 12 illustrates the configurations of mechanisms at GCP 65% when the uppermost joints achieve their peak altitude angles. Fig. 12 also displays the corresponding altitude angle values. The compactness values of the mechanisms are sequentially ordered from least to most, beginning with 'R-4B-R', and followed by the compactness associated with Case 1 (range), Case 2 (direction), and Case 3 (compactness). Fig. 12(a) demonstrates that a lower peak altitude angle, or more compact, correlates with a larger size of the mechanism in the altitude direction. Also, a comparison of Case 1 and Case 3 shows the trade-off between the compactness and range of moment variance in the sagittal plane. The trade-off is rooted in movements of links and joints close to the equator of the spherical surface relatively smaller while even the same amount of movements of them located at higher altitudes resulting in a larger difference in altitude direction. Therefore, to maximize direction variations on the sagittal plane, designers should carefully set minimum compactness regarding the wearer's body size and step width to minimize constraint margin.

VI. PROTOTYPE DEVELOPMENT AND EXPERIMENTAL VERIFICATION

It is impossible to completely transmit the output moments generated from the robot, which could be calculated from kinematic analysis in Section III-B. and are given in Section V-A., to the wearer due to the inherent compliance of human tissues and connection parts. It is important to find out the actual force transmitted to a wearer. In this section, we experientially measure the transmitted force by using a prototyped hip wearable robot and testing bench.

A. MECHANISM FABRICATION

We decided to fabricate the case 3(direction) mechanism among the synthesized mechanisms. In the design optimization process, we set the multi-objective for creating various solutions. However, to create and adjust a robot intended for use, compactness was prioritized. Case 1(range mechanism) is quite bulky, and case 2(compact) mechanism doesn't provide sufficient sagittal plane moment output.

Design considerations for the fabrication include 1) joint design, 2) layer design, 3) connection design as follows:

1) JOINT DESIGN

We utilized ball bearings and hinge pin couplings(MISUMI, standard parts) to ensure the axial rotation while withstanding bending moments applied perpendicular to the axis, which are
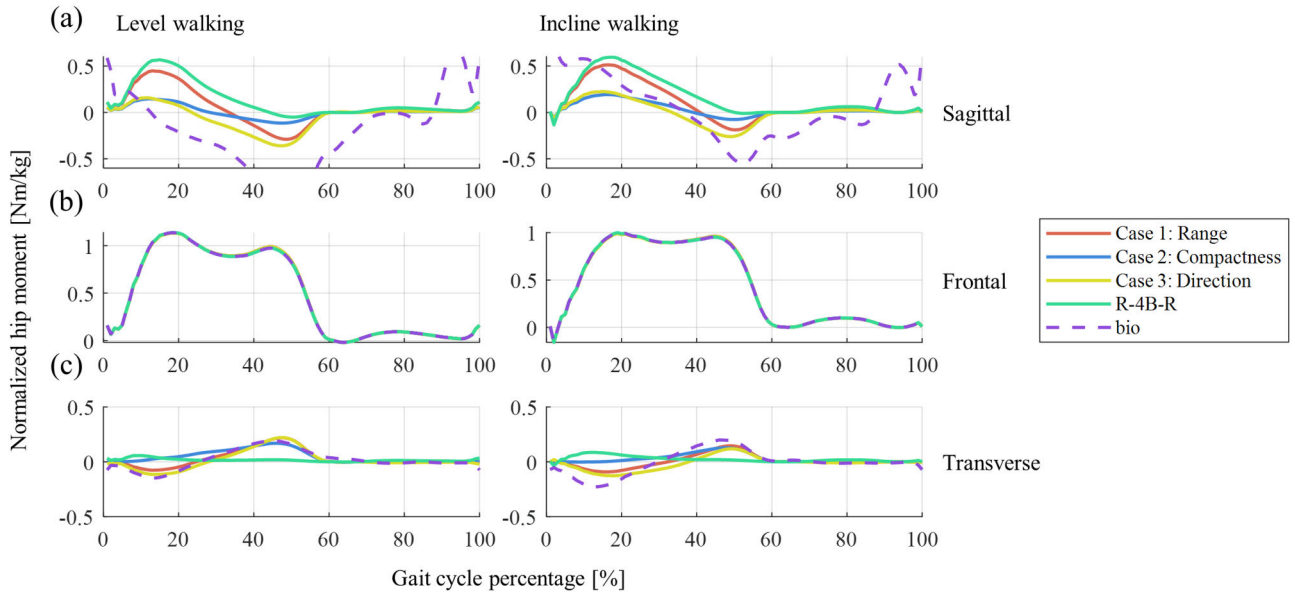
FIGURE 9. Moments generated by synthesized mechanisms. (a) in sagittal plane (b) in frontal plane (c) in transverse plane.
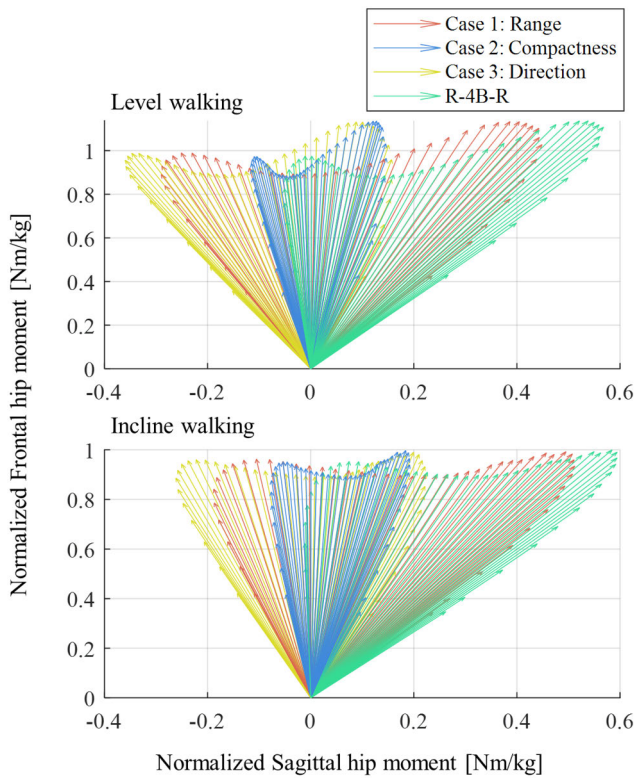

FIGURE 10. Output moment components in sagittal and frontal axes in single gait cycle. The output moments in the frontal plane remain constant across cases, whereas the sagittal moments show significant variation.

FIGURE 11. Virtual link trajectories of synthesized mechanisms and previous mechanism(R-4B-R) in the stance phase.

2) LAYER DESIGN

In the actual mechanism, the links are layered to avoid interference between links. Fig. 13(b) shows the links move separately in different radii of spheres. Increasing the number of layers increases the weight of the mechanism and the potential for interference with the human body. To minimize the number of layers, we positioned the end-effector closer to the leg by placing it on the smallest sphere and arranged the input links with increasing radii. To reduce the number of layers, some links were designed in an S-shape. This resulted in a compact design with 5 layers compared to the 4-bar mechanism, which has 4 layers for 5 links.

3) CONNECTION DESIGN

As Fig. 13(a) shows, the input link was designed to be flat towards the front to allow connection to a fixed part mounted on the body. We also designed it to accommodate torque sensors for measuring input moments. The end-effector

common in spherical mechanisms. Fig. 13(a) shows the inner side of the mechanism, with bearing in each joint. Fig. 13(b) shows the outer side of the mechanism, with a hinge pin in each joint.
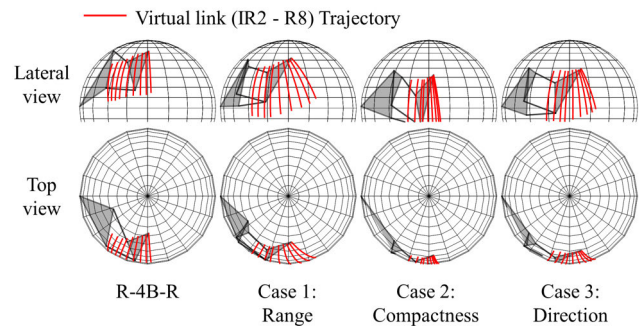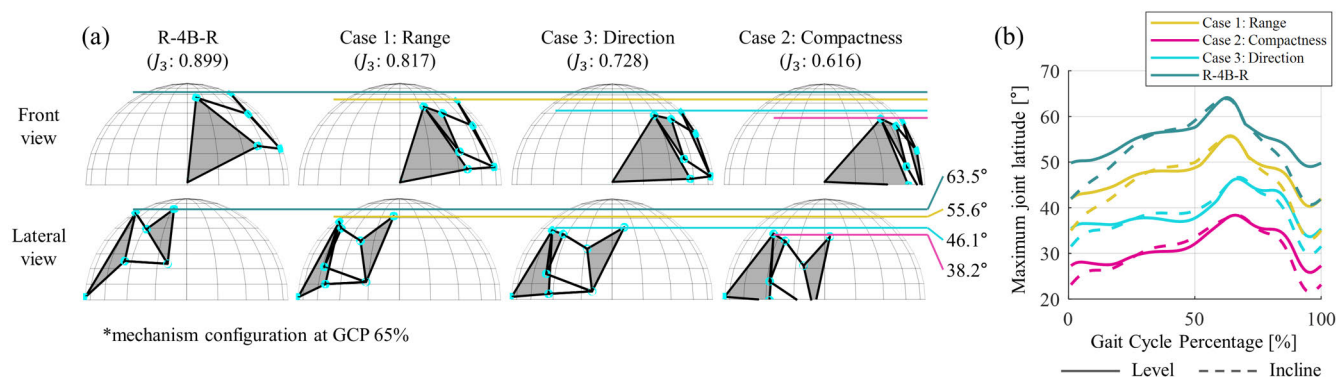
FIGURE 12. Compactness analysis of synthesized mechanisms and R-4B-R mechanism. (a) Different views of mechanism configurations where each of them is at its maximum altitude. (b) altitudes of highest joints of mechanisms across gait cycle.

included a thigh connection part with a pipe, including a full bridge strain gauge that could measure bending moments in three axes, ensuring attachment to the human leg for fixation.

B. BENCH TEST IMPLEMENTATION

We implement a bench test to verify the output moment and range of motion of the fabricated hip joint mechanism and to validate its safety. This test bench is designed to share similar connection parts with the actual robot for a realistic environment. Fig. 13(a) shows the form of the test bench with the implemented mechanism on the left and the components of the distal part on the right.

1) MECHANISM CONNECTING PARTS AND ARTIFICIAL LEG

A flexible shaft, not shown in the photos, connects the input link of the mechanism to the motor. The mechanism's end effector is connected to the thigh part of the exoskeleton robot. The thigh part is designed with a special cable pattern using the previous approach [9] to effectively transmit combined moments in the frontal and sagittal directions. The artificial leg part is made up of a ball joint mount for cameras(Horusbennu, FX-45T) and a 3D-printed artificial thigh with silicon skin. Fig. 13(b) illustrates the movement of the mechanism and the artificial thigh according to the leg's rotation angle.

2) SENSORS AND ACTUATION SYSTEM

We constructed the system of the test bench, which includes digital and analog sensors and drivers, using the previous approach [22]. Data collection from the sensors and motor control in the test bench is achieved using NI's compactRIO-9042. The motor (Komotek, KAFZ-08DF6N21) is rated at 750W with a peak torque of 4.8 Nm and a gear ratio of 10:1, allowing for a maximum input torque of 48 Nm. Analog signals from the torque sensor (Futek, TFF350) for measuring input moments and a custom-ordered 3-channel strain gauge (Dacell) for measuring 3D output moments are amplified (Futek, IAA-100) and transmitted as 0-10V analog voltage

signals. An IMU (Xsens, mti-630) mounted on the artificial thigh records the current angle of the artificial thigh.

3) CONTROLLER

The input moments of the mechanism are generated by using a closed-loop admittance control strategy [8], [23]. This strategy takes into account the compliance of the flexible shaft used to transmit power from the motor to the test bench. The admittance model converts the desired torque into a desired target velocity. For low-level control, a PID controller regulates motor currents in proportion to the target velocity.

4) MOMENT TRANSMISSION PATH

The power generated by the motor is transmitted through a flexible shaft to the static torque sensor connected to the mechanism, as shown in Fig 13(a). In this diagram, the moment is transmitted in the following sequence: actuator - flexible shaft - torque sensor - R6Sbar-R mechanism - pipe with the robot strain gauge attached - artificial thigh.

C. BENCHTOP EXPERIMENT

1) EXPERIMENT PROCESS

For the experiments, the range of hip joint angles was determined using the maximum/minimum ranges of walking data on flat and sloped surfaces [14]. The experimental points were determined using Latin Hypercube Sampling within the experimental range to consider spatial compactness. Table 3 shows 15 hip joint angles extracted through Latin Hypercube Sampling [24], to ensure the equality of distributed sample points among dimensions.

The experimental procedure is as follows:

1) Calibrate the IMU.
2) Set the artificial leg angles according to the predefined hip joint angles. The mechanism moves along with the artificial thigh.
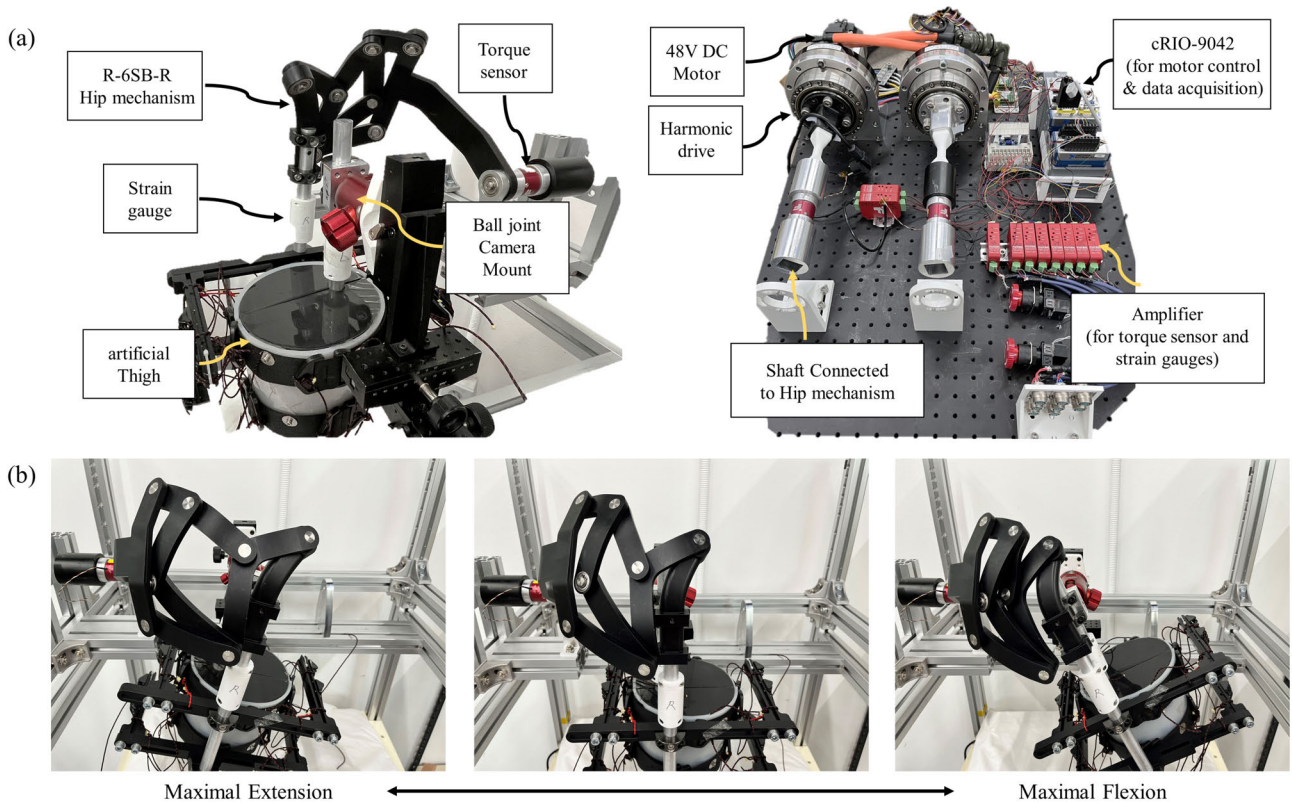3) Apply input moments, whose magnitude continuously changes from -3Nm to 3Nm, to the mechanism.

FIGURE 13. The test bench system. (a) The physical system contains a ball joint, artificial thigh, mechanism, and sensors. The electrical system contains motors, controllers, and amplifiers for sensors. (b) Various postures of 3-DOF Hip joint mechanism during benchtop test.

TABLE 3. The experimental point of hip joint angle in degree(°) extracted by Latin Hypercube sampling.

	Sagittal	Frontal	Transverse
1	16.17	-6.17	0.18
2	37.90	-4.41	0.18
3	1.69	-5.29	0.18
4	-5.55	-0.87	0.18
5	27.04	0.02	0.18
6	34.28	-1.75	0.18
7	23.41	2.67	0.18
8	45.14	-7.94	0.18
9	30.66	1.79	0.18
10	19.79	-8.83	0.18
11	8.93	-7.06	0.18
12	-1.93	-9.71	0.18
13	41.52	-2.64	0.18
14	5.31	0.90	0.18
15	12.55	-3.52	0.18

*All hip moments in this paper are normalized, (Nm/kg).

4) Return to 0Nm input moment and repeat the process for different hip angles.

The mechanism's output moments are measured using a 3-channel strain gauge attached to the robot's pipe, in Fig. 13(a). Each channel measures voltage proportional to bending moments in the coordinate of the robot's artificial leg. he measured voltage signal contains not only a signal from the moment transmitted by the mechanism but also a signal from the moment resulting from the robot's own weight. Therefore, after adjusting the angle and measuring the voltage at 0 Nm input moment, it is subtracted from the voltage at 3 Nm input moment. Then, a coordinate system rotation transformation according to the hip angle and a calibration matrix transformation for moment conversion are applied sequentially. Both transformations are linear.

2) EXPERIMENT RESULTS

Fig. 14 shows the theoretical moments and the moments obtained in the experiment when input moments from -3 Nm to 3 Nm were applied. Each column represents the three directions of hip joint moments, and the first row shows the theoretical moments obtained from the kinematic equation in 4, while the second row shows the moments obtained in the experiment. Each line corresponds to a result for each hip angle. The total number of hip angles is 15, and the relation between the color of lines and hip angles is shown in Fig. 14 as legend.

Experimentally measured moments are overall well matched with theoretical moments except the results under input moments with the magnitude of -3Nm to -2Nm. The magnitude of experimental output moments tends to be decreased near 0.3 to 0.6Nm. This might be because of interference between the patterned cables utilized to effectively transmit spatial moments and the buckle on the
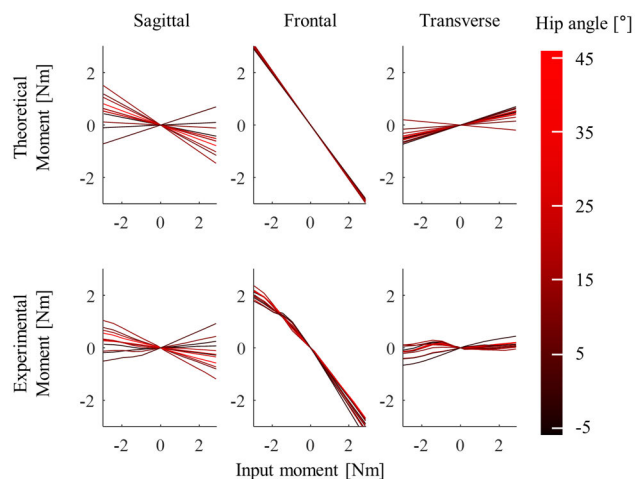
FIGURE 14. Comparison of the theoretical and experimental output moment.

artificial leg. This interference issue needs to be addressed in future designs.

Meanwhile, in the transverse plane, overall experimental results are distorted from the theoretical expectations. This error is assumed to come from the measurement error of the z-axis strain gauge. The rotation axis of the strain gauges on the pipe does not pass the center of the hip joint, resulting in an unnecessary coupling effect of measurement between transverse and sagittal. The measurement setup could be improved in future research.

In conclusion, we successfully validated that the designed mechanism could deliver the output moments in the intended direction to the wearer, even considering skin compliance, modeled with silicone and cable connection compliance, under benchtop test conditions.

VII. CONCLUSION

This paper introduces a systematic design and verification approach for a single-actuator hip exoskeleton mechanism capable of transmitting fixed-direction input torque into spatially varying assistance moments in both the frontal and sagittal planes using only one actuator. Our approach includes target-cascading from real-human gait data, manual type synthesis, multi-objective linkage shape optimization using NSGA-II, and experimental verification through prototyping and benchtop tests. This process allows for designs focused on the compactness of the mechanism to prevent interference with the human body, output moment direction accuracy to human biological data, and range of sagittal output moment to ensure sufficient forward propulsion performance, depending on specific design priorities. The R-6SB-R hip mechanism, a notable outcome of our work, surpasses the previously proposed R-4B-R mechanism [13], supporting a wider range of daily activities such as level and incline walking in a more compact design.

Future work will involve clinical experiments to verify the mechanism's assistive performance on humans and

the development of control methods for it. Ultimately, we believe this framework will significantly advance the use of mechanism-integrated exoskeleton robots, facilitating the creation of cost-effective, lightweight, and personalized assistive devices.

REFERENCES

[1] P. W. Franks, G. M. Bryan, R. Reyes, M. P. O'Donovan, K. N. Gregorczyk, and S. H. Collins, "The effects of incline level on optimized lower-limb exoskeleton assistance: A case series," *IEEE Trans. Neural Syst. Rehabil. Eng.*, vol. 30, pp. 2494–2505, 2022.

[2] G. M. Bryan, P. W. Franks, S. C. Klein, R. J. Peuchen, and S. H. Collins, "A hip–knee–ankle exoskeleton emulator for studying gait assistance," *Int. J. Robot. Res.*, vol. 40, nos. 4–5, pp. 722–746, Apr. 2021.

[3] J. Kim, B. T. Quinlivan, L.-A. Deprey, D. A. Revi, A. Eckert-Erdheim, P. Murphy, D. Orzel, and C. J. Walsh, "Reducing the energy cost of walking with low assistance levels through optimized hip flexion assistance from a soft exosuit," *Sci. Rep.*, vol. 12, no. 1, Jun. 2022, Art. no. 11004.

[4] Y.-T. Pan, I. Kang, J. Joh, P. Kim, K. R. Herrin, T. M. Kesar, G. S. Sawicki, and A. J. Young, "Effects of bilateral assistance for hemiparetic gait post-stroke using a powered hip exoskeleton," *Ann. Biomed. Eng.*, vol. 51, no. 2, pp. 410–421, Feb. 2023.

[5] A. J. Young, J. Foss, H. Gannon, and D. P. Ferris, "Influence of power delivery timing on the energetics and biomechanics of humans wearing a hip exoskeleton," *Frontiers Bioeng. Biotechnol.*, vol. 5, p. 4, Mar. 2017.

[6] C. L. Dembia, A. Silder, T. K. Uchida, J. L. Hicks, and S. L. Delp, "Simulating ideal assistive devices to reduce the metabolic cost of walking with heavy loads," *PLoS ONE*, vol. 12, no. 7, Jul. 2017, Art. no. e0180320.

[7] H. D. Yang, M. Cooper, A. Eckert-Erdheim, D. Orzel, and C. J. Walsh, "A soft exosuit assisting hip abduction for knee adduction moment reduction during walking," *IEEE Robot. Autom. Lett.*, vol. 7, no. 3, pp. 7439–7446, Jul. 2022.

[8] A. Alili, A. Fleming, V. Nalam, M. Liu, J. Dean, and H. Huang, "Abduction/adduction assistance from powered hip exoskeleton enables modulation of user step width during walking," *IEEE Trans. Biomed. Eng.*, early access, Aug. 4, 2023, doi: 10.1109/TBME.2023.3301444.

[9] V. L. Chiu, M. Raitor, and S. H. Collins, "Design of a hip exoskeleton with actuation in frontal and sagittal planes," *IEEE Trans. Med. Robot. Bionics*, vol. 3, no. 3, pp. 773–782, Aug. 2021.

[10] S. Sadeqi, S. P. Bourgeois, E. J. Park, and S. Arzanpour, "Design and performance analysis of a 3-RRR spherical parallel manipulator for hip exoskeleton applications," *J. Rehabil. Assistive Technol. Eng.*, vol. 4, Jan. 2017, Art. no. 205566831769759.

[11] Y. Yu and W. Liang, "Manipulability inclusive principle for hip joint assistive mechanism design optimization," *Int. J. Adv. Manuf. Technol.*, vol. 70, nos. 5–8, pp. 929–945, Feb. 2014.

[12] J. Beil and T. Asfour, "New mechanism for a 3 DOF exoskeleton hip joint with five revolute and two prismatic joints," in *Proc. 6th IEEE Int. Conf. Biomed. Robot. Biomechatronics (BioRob)*, Jun. 2016, pp. 787–792.

[13] S. W. Kang, J. Ryu, S. I. Kim, Y. Kim, and Y. Y. Kim, "Computational synthesis of wearable robot mechanisms: Application to hip-joint mechanisms," 2023, *arXiv:2308.11018*.

[14] R. Macaluso, K. Embry, D. J. Villarreal, and R. D. Gregg, "Parameterizing human locomotion across quasi-random treadmill perturbations and inclines," *IEEE Trans. Neural Syst. Rehabil. Eng.*, vol. 29, pp. 508–516, 2021.

[15] Ramon Sancibrian, Esther G Sarabia, Angel Sedano, and Jesus M Blanco, "A general method for the optimal synthesis of mechanisms using prescribed instant center positions," *Appl. Math. Model.*, vol. 40, no. 3, pp. 2206–2222, 2016.

[16] J. M. McCarthy and G. S. Soh, *Geometric Design of Linkages*, vol. 11. Cham, Switzerland: Springer, 2010.

[17] R. Je-Kyung, "(The) optimal hip mechanism for minimized metabolic cost during loaded walking in a single actuated lower limb exoskeleton robot /Ryu Je-Kyung [electronic resource]," Tech. Rep., 2022.

[18] K. Deb, A. Pratap, S. Agarwal, and T. Meyarivan, "A fast and elitist multiobjective genetic algorithm: NSGA-II," *IEEE Trans. Evol. Comput.*, vol. 6, no. 2, pp. 182–197, Apr. 2002.

[19] J. Badduri, R. A. Srivatsan, G. S. Kumar, and S. Bandyopadhyay, "Coupler-curve synthesis of a planar four-bar mechanism using NSGA-ii," in *Proc. Asia–Pacific Conf. Simulated Evol. Learn.* Cham, Switzerland: Springer, 2012, pp. 460–469.

[20] J. A. Joines and C. R. Houck, "On the use of non-stationary penalty functions to solve nonlinear constrained optimization problems with GA's," in *Proc. 1st IEEE Conf. Evol. Computation. IEEE World Congr. Comput. Intell.*, Jun. 1994, pp. 579–584.

[21] J. G. Hobbie, A. H. Gandomi, and I. Rahimi, "A comparison of constraint handling techniques on NSGA-II," *Arch. Comput. Methods Eng.*, vol. 28, no. 5, pp. 3475–3490, Aug. 2021.

[22] J. Ryu, S. Yang, and G. Lee, "Single actuator with versatile controllability of 2-DOF assistance for exosuits via a novel moving-gear mechanism," *Actuators*, vol. 11, no. 5, p. 135, May 2022.

[23] G. Lee, Y. Ding, I. G. Bujanda, N. Karavas, Y. M. Zhou, and C. J. Walsh, "Improved assistive profile tracking of soft exosuits for walking and jogging with off-board actuation," in *Proc. IEEE/RSJ Int. Conf. Intell. Robots Syst. (IROS)*, Sep. 2017, pp. 1699–1706.

[24] M. D. McKay, R. J. Beckman, and W. J. Conover, "A comparison of three methods for selecting values of input variables in the analysis of output from a computer code," *Technometrics*, vol. 21, no. 2, p. 239, May 1979.

GYUIK LEE received the B.S. degree in mechanical engineering from Chung-Ang University, Seoul, South Korea, in 2021, and the M.S. degree in mechanical engineering from Seoul National University, Seoul, in 2023. His research interests include the mechanisms and exoskeleton design.

JEONGHAN YU received the B.S. degree in mechanical engineering from Seoul National University, Seoul, South Korea, in 2017, where she is currently pursuing the Ph.D. degree in mechanical engineering. Her research interests include the autonomous design of linkage mechanisms and the design and control of exoskeletons.

JONGJUN LEE received the B.S. degree in mechanical engineering from Seoul National University, Seoul, South Korea, in 2017, where he is currently pursuing the Ph.D. degree in mechanical engineering.

His research interests include the design optimization of linkage mechanisms and exoskeleton design.

SEOK WON KANG received the B.S. and Ph.D. degrees in mechanical and aerospace engineering from Seoul National University, Seoul, South Korea, in 2014 and 2020, respectively. He was a Postdoctoral Researcher with the Institute of Advanced Machines and Design, Seoul, until 2021. He is currently a Postdoctoral Fellow with Johns Hopkins University, Baltimore, MD, USA. His research interests include topology optimization, linkage mechanisms, wearable robotics, and additive manufacturing.

JEGYEONG RYU received the B.S. and M.S. degrees in mechanical engineering from Seoul National University, Seoul, South Korea, in 2020 and 2022, respectively, where she is currently pursuing the Ph.D. degree in mechanical engineering. She was an Intern Researcher with the Korea Institute of Science and Technology, Seoul, until 2022. Her research interests include medical robots, soft robots, and image-guided surgeries.

YOON YOUNG KIM received the B.S. and M.S. degrees from Seoul National University, Seoul, South Korea, in 1981 and 1983, respectively, and the Ph.D. degree in mechanical engineering from Stanford University, Stanford, CA, USA, in 1989. He started his academic career with Seoul National University, in 1991. He is currently a Distinguished Professor.

• • •